



Late Quaternary normal faulting within the rigid Ili Basin: Insights into the deformation pattern of the northern Tian Shan, NW China

Chuanyong Wu ^{a,b,c,*}, Haiyang Yuan ^a, Kezhi Zang ^a, Sihua Yuan ^{a,b}, Xiangdong Bai ^{a,b}, Chengyao Guan ^{a,b}, Peizhen Zhang ^d, Zhan Gao ^a, Xuezhu Wang ^a

^a Institute of Disaster Prevention, Langfang, 065201, China

^b Hebei Key Laboratory of Earthquake Dynamics, Langfang, 065201, China

^c Xinjiang Pamir Intracontinental Subduction National Observation and Research Station, Beijing, 100029, China

^d Guangdong Provincial Key Laboratory of Geodynamics and Geohazards, School of Earth Sciences and Engineering, Sun Yat-sen University, Guangzhou, 510275, China

ARTICLE INFO

Handling Editor: Dr Giovanni Zanchetta

Keywords:

Tian Shan

Ili Basin

Yamadu fault

Late Quaternary normal faulting

Crustal rotation

ABSTRACT

The deformation pattern of the Tian Shan orogenic belt associated with the ongoing India–Eurasia collision is poorly understood due to the lack of deformation of the intermontane basins embedded in the mountains. The Yamadu Fault is a NW-striking structure in the interior of the rigid Ili Basin and has clearly experienced tectonic deformation. In this study, we quantified its late Quaternary activity based on interpretations of detailed high-resolution remote sensing images and field investigations. Observations from four field sites along the ~70-km-long structure indicate that the Yamadu fault is characterized by normal faulting and exhibits a southeastward decrease in deformation rate along its strike. By surveying the displaced geomorphic surfaces with an unmanned drone and dating the late Quaternary sediments via optically stimulated luminescence, we estimate a maximum late Quaternary vertical slip rate of 0.37 ± 0.08 mm/yr and an E–W extension rate of 0.19 ± 0.08 mm/yr at the northwesternmost extent of the fault. The Yamadu Fault represents a boundary structure accommodating counterclockwise rotation and relative divergence between the Ili block and Tian Shan Mountains caused by right-lateral faulting at the northern margin of the basin. The Cenozoic deformation of the Tian Shan area included continuous deformation via the overwhelming crustal shortening accommodated by the soft lithospheric structure and a block-like deformation pattern of lateral extrusion and/or rotation accommodated by the rigid intermontane basin.

1. Introduction

Mountain-building and crustal deformation within the Asian continent are closely related to the integrity and strength of the lithospheric structure (Molnar and Tapponnier, 1981), which has obvious inheritance, as manifested by the presence of essentially undeformed cratons of the Tarim, Junggar and Kazakh blocks since the Paleozoic and the Cenozoic-reactivated Tian Shan orogenic belt (Allen et al., 1993; Burtman, 1975; Molnar and Tapponnier, 1981; Windley et al., 1990; Xiao et al., 2015). The actively deforming Tian Shan Mountains host numerous east–west (E–W) elongated intermontane basins, which have been proposed to be former Paleozoic microcontinents or blocks (Allen et al., 1993; Charvet et al., 2011; Windley et al., 1990). In stark contrast to the strong deformation and uplift of the surrounding ranges, the fault-bounded intermontane basins with Cenozoic sedimentary fill

present relatively flat landscapes (Fig. 1a). Previous research has suggested that intermontane basins behave more or less as rigid units and undergo localized shortening deformation at their margins (Avouac and Tapponnier, 1993; Thompson et al., 2002; Wang and Shen, 2020; Yang et al., 2008). In a compressive stress environment, a rigid intermontane basin should experience compressive-flexing deformation because of material loading or lateral extrusion motion (Tapponnier and Molnar, 1979; Avouac et al., 1993). In addition, strong uplift of the ranges and the consequent influence of gravitational potential energy result in deformation being transferred into the basin interior and destroying the basin structure (England and Houseman, 1985; Goode et al., 2014; Gebhardt et al., 2017). However, detailed studies focused on the deformation of rigid intermontane basins in the Tian Shan Mountains have rarely been reported to date. Therefore, investigating the internal deformation of intermontane basins embedded in mountains is essential

* Corresponding author. Institute of Disaster Prevention, Langfang, 065201, China.

E-mail address: cywueq@163.com (C. Wu).

for determining the deformation pattern of the Tian Shan orogenic belt and understanding the dynamics of continental mountain-building movement.

The triangular Ili Basin, the largest intermontane basin within the northern Tian Shan, has been interpreted as a rigid block with over-thrusting of Paleozoic bedrock upon the basin (e.g., Grützner et al., 2017; Luo et al., 2003). However, active faulting investigations (e.g., Feng, 1997; Grützner et al., 2019; Wu et al., 2020) indicate that the Ili Basin is bounded by several strike-slip faults to the north and west. To the north of the basin, the WNW-striking fault shows right-lateral slip (Feng, 1997; Wu et al., 2020); however, several NE-striking structures along the western boundary of the basin exhibit left-lateral motion (Grützner et al., 2019). Obviously, the deformation pattern of the Ili Basin significantly differs from previous observations of compressive-flexing deformation. Global position system (GPS) measurements (e.g., Wu et al., 2021; Zubovich et al., 2010) reveal a noticeable amount of tectonic extension deformation within the Ili Basin, implying some crustal deformation patterns that were previously not noticed or known in this region. In addition, field investigations (Luo et al., 2003) and seismic activity within the Ili Basin (Fig. 1b) suggest that the Ili block underwent tectonic deformation in its interior (Grützner et al., 2019), which contradicts the conventional deformation understanding of rigid blocks. In the interior of the Ili Basin, a NW-striking fault structure, named the Yamadu Fault (YF), displays well-expressed traces of active faulting at late Quaternary geomorphic surfaces (Fig. 1c). In contrast to the widespread thrust faults and folds under the nearly north–south (N–S) compression-dominated stress field, the YF exhibits evidence of normal faulting in the late Quaternary (Luo

et al., 2003). However, no quantitative studies on its geometry, late Quaternary deformation features or slip rates are available to decipher its tectonic role in the regional deformation and strain accommodation associated with the ongoing India–Eurasia collision.

In this study, we utilized high-resolution image interpretations and field investigations to describe the geometry and late Quaternary kinematics of the YF. Then, by surveying deformed geomorphic surfaces with an unmanned aerial vehicle (UAV) and dating the ages of the sediments through the optically stimulated luminescence (OSL) method, we estimated the fault slip rate and quantified the variations in fault kinematics along the fault strike; finally, we explored its role and implications for tectonic deformation in the northern Tian Shan orogenic belt. These results provide new insights into the crustal deformation and dynamics of intracontinental orogenic belts.

2. Regional tectonic setting

The Tian Shan orogenic belt was formed by the amalgamation of several Paleozoic tectonic units, including microcontinents, island arcs and accretionary wedges (Allen et al., 1993; Burtman, 1975; Windley et al., 1990; Xiao et al., 2015). In the Late Devonian to early Carboniferous, the first Tian Shan orogeny accreted a passive continental margin along the southern Tian Shan suture on the northern side of the Tarim Basin. The second Paleozoic orogeny accreted an active continental margin along the northern side to the northern Tian Shan island arc (Allen et al., 1993). The subsequent Permian to Mesozoic intracontinental extension and transtensional faulting created the regional tectonic framework in the Tian Shan region (Wang et al., 2007). The

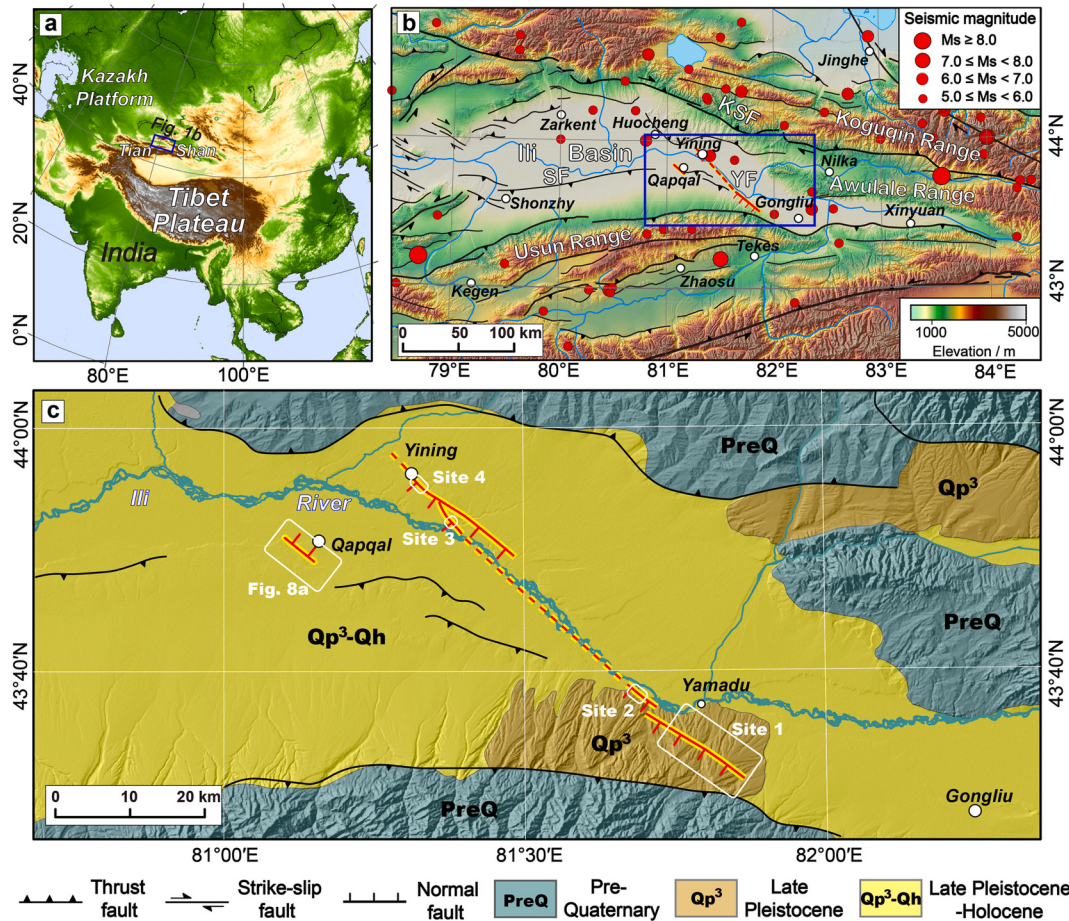


Fig. 1. (a) Tectonic location of the northern Tian Shan orogenic belt within the Eurasian continent. (b) Distribution of major active faults and seismicity with magnitudes greater than M_s 5 in the Ili Basin and its surrounding region. (c) Major active faults within the Ili Basin (fault data are modified from Luo et al., 2003; Wu et al., 2019; 2020). Seismicity data and topographic relief data are from Wu et al. (2020). KSF: Kashihe Fault; SF: Shonzhy Fault; YF: Yamadu Fault.

triangular Ili block embedded in the northern Tian Shan has a relatively strong basement and is composed of fault-bounded fragments of microcontinents (Allen et al., 1993; Charvet et al., 2011; Pelsmaeker et al., 2015). In addition to the boundary faults along the northern and southern margins of the Ili Basin, several NW-trending basement faults are present within the basin interior (Grützner et al., 2019; Zhang et al., 1999). In response to the India–Eurasia collision, surface uplift and basement exhumation in the Tian Shan initiated at ~24 Ma and became more pronounced at approximately ~11–10 Ma (Hendrix et al., 1994; Sobel et al., 2006), resulting in late Cenozoic sediments filling the foreland and intermontane basins. In the Ili Basin, widespread late Pliocene–early Pleistocene coarse clastics that unconformably cover Miocene strata indicate that significant range uplift and crustal shortening occurred after the Pliocene (Han et al., 2004).

The flat Ili Basin, which has an elevation of less than 1500 m, is surrounded by the Koguqin Range to the north and the Usun Range to the south (Fig. 1b). The elevations of the surrounding ranges reach more than 4000 m above sea level. Along the northern margin of the Ili Basin, the Kashihe Fault separates the pre-Cenozoic bedrock of the Koguqin range from the deformed Cenozoic layers in the basin; the Kashihe Fault underwent predominantly right-lateral faulting with thrust faulting components (Feng, 1997; Wu et al., 2020). Based on deformed alluvial fan surveying and OSL dating, Wu et al. (2020) estimated a slip rate of ~2 mm/yr for the Kashihe Fault. The southern margin of the Ili Basin, as demonstrated by previous geological studies (Grützner et al., 2017) and GPS measurements (Wu et al., 2023), is dominated by northward thrust faulting and accommodates N–S convergent strain. GPS measurements indicate that the NE-striking fault slips left-laterally at a rate of ~3 mm/yr to the west of the basin (Wu et al., 2021). In addition, several subparallel ENE-striking thrust faults and folds are present at the NW margin of the basin (Kober et al., 2013). Although the rate of late Quaternary crustal shortening on an individual ENE-striking fault is only 0.25 mm/yr (Cording et al., 2014), the cumulative GPS-derived shortening rate across these ENE-striking structures may be 1–3 mm/yr (Zubovich et al., 2010).

Within the basin interior, several E–W-striking structures, such as the Shonzhy Fault, have been reported and confirmed to have been active during the late Quaternary; these faults are interpreted as splay faults from the range-front structure (Grützner et al., 2019; Mackenzie, 2016).

Historical records of seismicity in the Ili region cover only the past ~300 years. Four large historical events with magnitudes greater than 6.0 have occurred in the Ili Basin region (Fig. 1b). The 1812 Ms 8 Nilka earthquake, the largest event in this region, generated approximately 80 km long surface ruptures with obvious dextral components along the northern margin of the Ili Basin (Feng, 1997; Yin et al., 2006). With respect to the 1786 Ms 6.5 Huocheng earthquake and the 1921 Ms 6.5 Yining earthquake in the basin interior, no further information about their focal mechanism and seismogenic faults is available because of the lack of seismic phase data and historical records. However, earthquake damage records indicate that these events occurred in the basin interior. The recent 2011 Ms 6.0 Gongliu event at the southern margin of the basin was dominated by thrust motion (Wang et al., 2013), which is consistent with fault kinematics in this part of the basin. In addition to several large earthquakes on the boundary structures of the Ili Basin, instrumental records reveal that ten earthquakes greater than 5.0 have occurred in the last 230 years within the basin interior (Fig. 1b), indicating that a portion of convergent strain is accommodated within the rigid Ili Basin (Zubovich et al., 2010; Wu et al., 2021).

3. Methods

3.1. High-resolution remote sensing image interpretations, field mapping and surveying observations

In this study, we utilized high-resolution remote sensing images to interpret and map deformed geomorphic surfaces and fault traces to

observe the geometry of the YF. Our interpretations at several key sites were based on Google Earth images and high-resolution digital elevation model (DEM) data surveyed by a UAV. The UAV platform used (DJI Phantom 4 RTK) was equipped with a 20-megapixel imaging sensor. In the field, five or six ground control points (GCPs) that consisted of 50 cm square red and white papers were evenly spread across the study area before photographs were acquired. The GCP locations were surveyed via differential GPS with a horizontal error of 2 cm and a vertical error of 4 cm. Photos were collected with 70 % forward and 70 % side overlap to ensure common features between adjacent images, with a flight altitude of 150–180 m. A total of 1525 photos were utilized to create the final model via Agisoft PhotoScan software. Because of the sparse vegetation on the surface, our DEMs obtained via the structure-from-motion (SfM) technique (Westoby et al., 2012) had a resolution of <0.3 m/pixel. Finally, hillshade maps of ~1.9 km² for Site 1 and ~1.4 km² for Site 2 were created in ArcMap. To determine the late Quaternary kinematics of the YF, we surveyed and sampled along the fault scarp and cleaned several natural outcrops to describe the active deformation in detail.

We measured the fault displacements along the YF based on high-resolution DEM data and differential GPS data. The topographic profiles across the scarps were constructed roughly perpendicular to the strike of the fault. We fit these profiles and straight lines above and below the scarp to obtain the vertical displacements across the fault, and the errors mainly result from the uncertainty of line fitting (Thompson et al., 2002). To define the variations in the fault kinematics along its strike, we compared the vertical slip rates and extension rates determined from the fault dip at different study sites.

3.2. Age dating

In the Ili Basin region, fine sand and/or silt lenses in alluvial gravel and eolian loess overlying geomorphic surfaces provide materials for OSL dating, which is widely used in the arid and semiarid Tian Shan region. Our OSL sample preparation and analysis were performed at the State Key Laboratory of Earthquake Dynamics, Institute of Geology, China Earthquake Administration (CEA). The samples were extracted from the inner unexposed part of the tubes, and the quartz was purified via conventional sample preparation techniques (dissolving carbonates with 10 % HCl, oxidizing organic matter with 10 % H₂O₂, settling via Stokes' law, dissolving feldspars with 30 % fluorosilicic acid for three days, followed by immersion in 10 % HC) to obtain the 4–11 µm fine-grained quartz (FQ) fraction (Aitken, 1998; Liu et al., 2010). The purity of the quartz extracts was confirmed by the absence of an IRSL signal for FQ. Subsamples of FQ had IR signals close to background levels, with an IR-OSL depletion ratio between 0.9 and 1.1 (Duller, 2003). The 90–180 µm coarse-grained feldspar (CKF) fractions were obtained via wet sieving and heavy liquid separation, and etching with 10 % HF for 15 min was conducted.

All the De values of the samples were measured on a Risø TL/OSL Reader model DA-20 equipped with a calibrated ⁹⁰Sr/⁹⁰Y beta radiation source (dose rate of 0.1125 Gy/s in the standard configuration), blue (470 ± 30 nm; ~50 mW/cm²) and infrared (880 ± 40 nm, ~145 mW/cm²) light sources, and detected through a U-340 glass filter for FQ and BG-39 for CKF. The FQ fractions were measured via a sensitivity-corrected (by a test dose) multiple-aliquot regenerative-dose (SMAR) protocol (Lu et al., 2007; Yang et al., 2017). At least six aliquots were measured to determine the natural OSL intensity, and a dose-response curve (DRC) was constructed from six aliquots that bracketed the natural (normalized) OSL signals.

For the De measurements of CKF, we employed a postinfrared (IR)-stimulated luminescence (IRSL) SAR protocol (pIRIR 225; Buylaert et al., 2011). After preheating at 250 °C for 60 s, the aliquots were stimulated twice with IR diodes for 200 s. During the first stimulation, the temperature was maintained at 125 °C (IR signal), whereas the second IR stimulation temperature was maintained at 225 °C (post-IR IRSL signal, pIRIR 125, 250), during which the signal of interest was

recorded. The CKF post-IR IRSL signals were derived from the initial 2.0 s of stimulation, which was less than the background from the last 5.0 s. At least six aliquots for every sample were measured, and the over-dispersions of De values were less than 5 %. A central age model was used to calculate the equivalent dose for FQ and CKF.

4. Observations and results along the YF

4.1. Geometry and late quaternary kinematics of the YF

We conducted detailed field investigations and surveying observations along the ~70 km-long fault. The YF is unrecognized along the Ili River valley; therefore, we focused on the southeastern and northwestern sections of the YF to quantify its late Quaternary kinematics. In this section, we describe in detail four investigation sites numbered one to four from east to west (Fig. 1c) and report the fault geomorphology, kinematics and displacements.

4.1.1. Site 1

South of the town of Yamadu, a late-Pleistocene alluvial fan is widely developed in the Usun Range piedmont (Luo et al., 2003). This geomorphic surface has been incised by a series of roughly N–S flowing gullies with maximum widths of up to 300–500 m, but the surface remnants of this alluvial fan remain flat (Fig. 2a). On the piedmont alluvial fan, we observed well-expressed fault scarps that trend NW and extend approximately 20 km long. The SW-facing scarp has displaced geomorphic surfaces with different vertical displacements along the fault strike. Near the southeastern end of the fault, the vertical displacement of the counter slope fault scarp is only ~1.5–2.0 m

(Fig. 2b). Northwestward, approximately 4.5 km along the fault strike, the fault trace shows a well-expressed linear expression in the satellite imagery (Fig. 2a). The high-resolution SfM model provides a detailed image of the fault trace and deformed geomorphic surfaces. The SW-facing fault scarp crosses the late-Pleistocene alluvial fan and several levels of river terraces of the Jamante River, a roughly N–S flowing tributary of the Ili River. The vertical displacement recorded by the piedmont alluvial fan is approximately 12.5–15.7 m (Fig. 2c), which is much greater than that recorded at the southeastern tip of the YF.

4.1.2. Site 2

To the southwest of Yamadu, the fault trace is clearly expressed on the late Quaternary geomorphic surfaces. The YF exhibits good evidence of vertical faulting and forms a SW-facing scarp at the surface (Fig. 3a). Jurassic coal-bearing sandstone is exposed on the northern block (footwall) of the fault (Fig. 3b–d). Coal mining revealed that the YF is a high-angle normal fault dipping south at ~60–70° and displaces the late Quaternary alluvial gravel layer (Fig. 3b and c). Roughly vertical fault slip striations can be clearly observed on the fault surface (Fig. 3c). On the late Quaternary alluvial fan, several ephemeral channels with widths of 30–50 m flow northward to the Ili River. Two main grades of alluvial terraces can be identified along the NNE-trending river valley, which have been displaced by the YF (Fig. 3a). The T1 and T2 terraces and the alluvial fan are ~25 m, 35 m and 50 m above the riverbed, respectively. Field investigations and high-precision DEMs created from UAV surveys indicate that the three levels of geomorphic surfaces have been displaced across the fault. Although the T2 terrace and alluvial fan have been artificially modified on the north side (footwall block) of the fault, the remnants of the T2 terrace and alluvial fan surface can still be

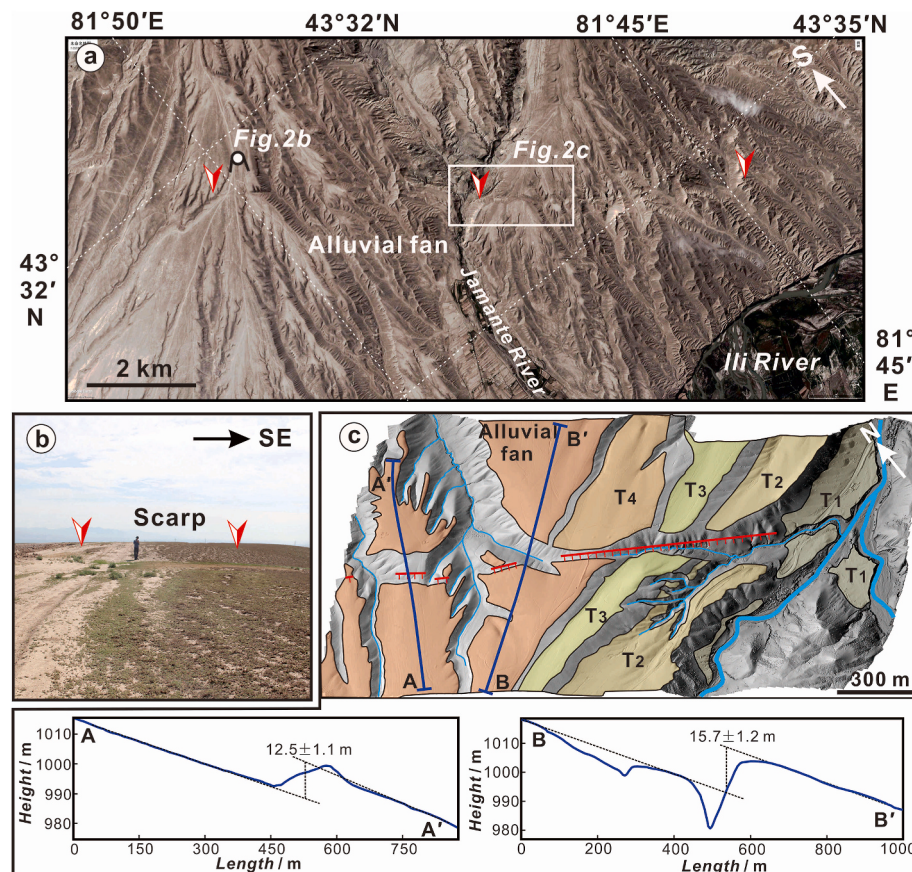
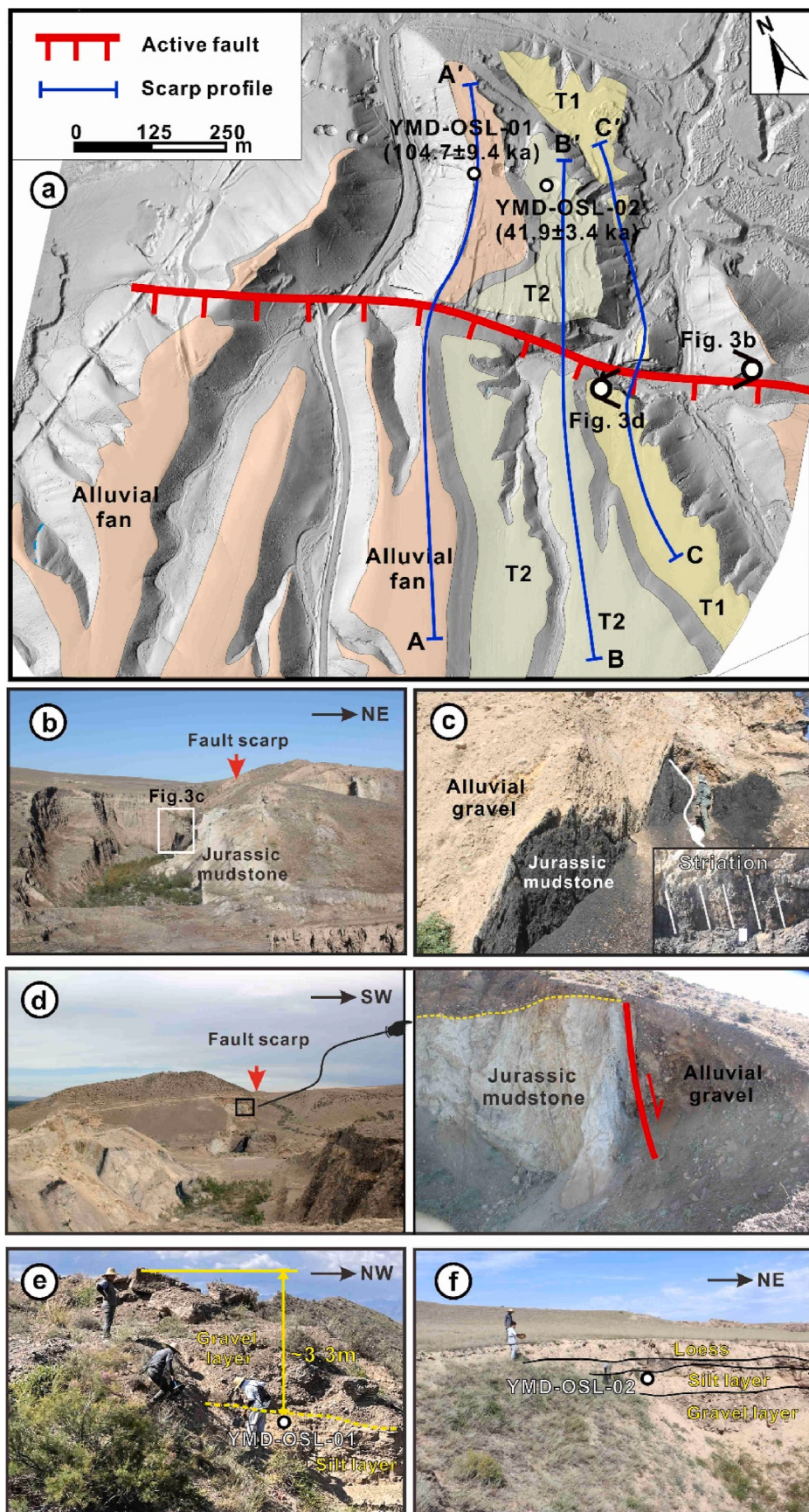


Fig. 2. (a) High-resolution remote sensing image obtained from Google Earth showing the fault traces (marked by red arrows) on the piedmont alluvial fan. (b) Photograph taken facing ~ NE showing a vertical scarp with heights of ~1.5–2.0 m at the alluvial fan. (c) DEM surveyed by a UAV (the uninterpreted image is provided in the supplement) showing the fault trace and the displaced geomorphic surfaces. Two topographic profiles across the scarp show vertical displacements.



(caption on next page)

Fig. 3. (a) DEM surveyed by a UAV (the unannotated image is provided in the supplementary material) showing the faulted geomorphic surfaces near the town of Yamadu. The alluvial fan and terraces record the vertical displacement of the YF. (b) Photograph taken facing ~NW showing the southwest-down scarp (marked by red arrows) on the late Quaternary geomorphic surfaces. (c) Photographs (see panel b for the location) showing the fault section. The YF is a high-angle normal fault dipping south at ~60–70°. Vertical fault slip striations on the fault surface imply the kinematics of the YF. (d) Photographs showing the southwest-down scarp (marked by red arrows) on the alluvial fan and the fault outcrop. (e) Photograph taken facing approximately south showing the sediments of the alluvial fan and the sample location of YMD-OSL-01. (f) Photograph taken facing approximately NW showing the sediments of the T2 terrace and the sample location of YMD-OSL-02.

identified, which can therefore be viewed as markers to estimate the vertical displacements of the fault. The topographic profile across the fault scarp reveals that the vertical displacement of the alluvial fan is $\sim 15.2 \pm 2.0$ m (Fig. 4). The T2 terrace surface is mostly flat and wide; therefore, we effectively constrained the vertical slip displacement to $\sim 9.1 \pm 1.8$ m based on the high-resolution DEM (Fig. 4). The T1 terrace is discontinuous on the footwall block of the fault. Therefore, the T1 measurements must be taken with caution. We fit the surficial lines above and below the scarp to obtain a vertical displacement of approximately 3.6 m at the T1 terrace (Fig. 4). The scarp heights become progressively larger as the ages of the terraces become older, indicating that continuous deformation on the YF has occurred since the late Quaternary.

On the alluvial fan, we collected one fine sand sample of YMD-OSL-01 from the alluvial sediments at a depth of ~330 cm (Fig. 3e) for OSL dating. The analytical result of 104.7 ± 9.4 ka ($\pm 1\sigma$) represents the maximum abandonment age of the alluvial fan. On the T2 terrace, approximately 1.0-m thick aeolian loess covers the alluvial gravels. In the upper part of the gravel layer, we found an alluvial silty interlayer that was ~1.0–1.3 m thick. The OSL sample of YMD-OSL-02 was taken at a depth of ~190 cm from the upper deposition of the silty layer (Fig. 3f). The analytical result of 41.9 ± 3.4 ka represents the maximum abandonment age of the T2 terrace.

4.1.3. Site 3

In the Ili Basin, the late Quaternary alluvial fan, which constitutes

the main geomorphic surface, is widely developed (Fig. 1c). Near the Jilglang River, a tributary of the Ili River, two main alluvial fans, Fan1 and Fan2, have been identified based on their superposition and relative heights (Fig. 5a). The average surface elevation of Fan2 is obviously greater (~15–20 m) than that of Fan1. The YF displaced the late Quaternary alluvial fans to form SW-facing fault scarps, showing well-expressed traces in the Copernicus WorldDEM image (Fig. 5a). Here, the fault consists of north and south branches. The north branch fault strikes approximately N55°W and shows linear expression on the late Quaternary geomorphic surfaces (Fig. 5a). On Fan1, the vertical displacement of the scarp is approximately 3–4 m (Fig. 5b). West of the Jilglang River, the vertical displacement on the Fan2 surface is approximately 5–6 m (Fig. 5c). The southern branch fault strikes approximately N45°W and merges into the northern branch fault in the eastern suburbs of the city of Yining (Fig. 5a). The southern branch also displaced the late Quaternary alluvial fans to form a SW-facing scarp (Fig. 6a). A topographic profile across the fault scarp surveyed by differential GPS reveals that the vertical displacement on the Fan2 surface is 14.3 ± 0.8 m (Fig. 6c). A stratigraphic outcrop in a gravel quarry reveals that the alluvial sediments are covered by aeolian loess with a thickness of approximately 2.0–2.5 m (Fig. 6b). Between the aeolian loess and the alluvial gravels, a set of light brown silt layers that are ~0.9 m thick with horizontal bedding can be used for OSL dating. The YMD-OSL-05 sample was taken from the upper alluvium of the alluvial silt layer at a depth of ~260 cm (Fig. 6b). The analytical result of 65.0 ± 7.3 ka represents the maximum abandonment age of alluvial Fan2.

4.1.4. Site 4

Westward to the city of Yining, the alluvial fans have been transformed and covered by city buildings; however, the SW-facing fault scarp can still be distinguished on some well-preserved geomorphic surfaces (Fig. 7a, b and c). Therefore, the fault traces are discontinuous in terms of the fault geometry. Field investigations and surveys via differential GPS indicate that the vertical displacement of Fan1 by the YF is 11.2 ± 0.6 m (Fig. 7d). The northern side of the fault at Fan2 has a well-preserved landform; in contrast, the southern side of the fault at Fan2 has been transformed to build residential houses (Fig. 7a–c). Topographic profiles across the SW-facing scarp at Fan2 reveal that the vertical displacements of the fault are approximately 16.7–25.6 m (Fig. 7d). A natural stratigraphic section reveals that the alluvial sediments have a typical dual structure: the upper part is a set of 1.0–1.2 m-thick grayish yellow silt layers with horizontal alluvial bedding; the lower part is a set of gray black gravel layers. In addition, a set of 0.6–0.8 m-thick aeolian loess covers the alluvial deposits (Fig. 7e). The OSL sample of YMD-OSL-03 was taken from the bottom of the alluvial silt layer at a depth of 175 cm. The analytical result of 71.2 ± 7.1 ka for YMD-OSL-03 within the 1σ uncertainty (Table 1) restricts the maximum age for Fan2 abandonment.

4.2. The secondary NE-dipping normal fault within the Ili Basin

In addition to the SW-dipping YF normal structure, our field investigations revealed a secondary NE-dipping normal fault on the southern bank of the Ili River (Figs. 1c and 8a). On the river terrace of the Ili River near Qapqal County, the secondary normal fault strikes approximately N50–55°W and extends ~5 km along several topographic bulges approximately 4–7 m above the terrace surface (Fig. 8a). The fault trace is discontinuous and exhibits north-down motion in the

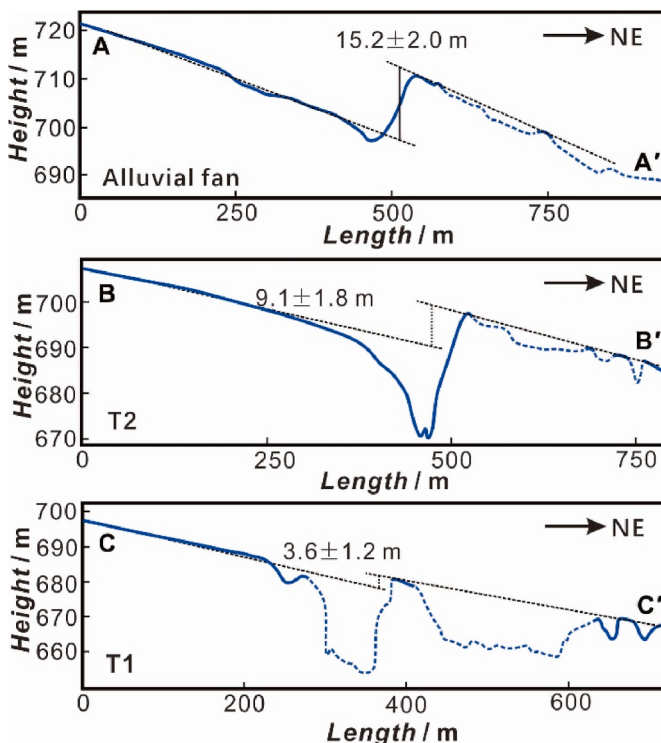


Fig. 4. Topographic profiles across the scarp showing vertical displacements of ~3.6 m, ~9.1 m and ~15.2 m at the T1 and T2 terraces and the alluvial fan, respectively (see Fig. 3a for the locations). Dashed lines representing the artificially modified areas.

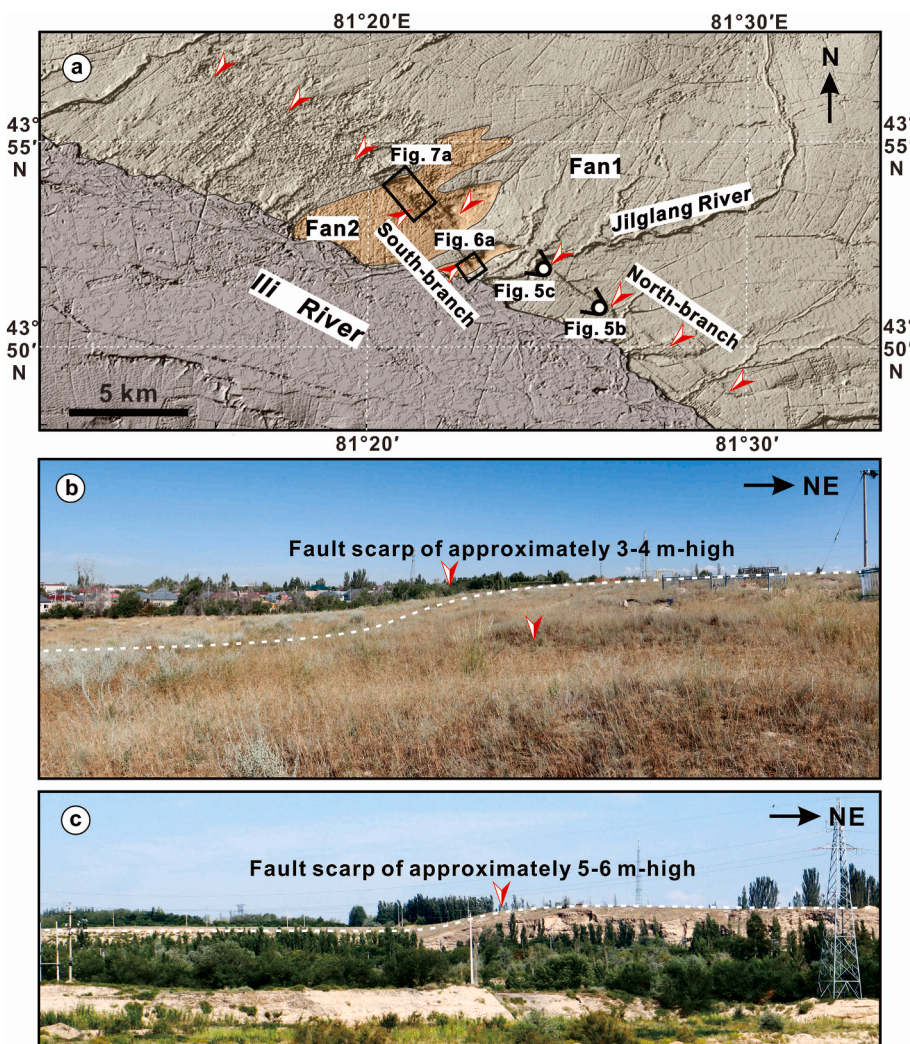


Fig. 5. (a) Copernicus WorldDEM with a resolution of 30 m showing fault geometry (marked by red arrows) near the city of Yining. (b) Photograph taken facing approximately NW showing the fault scarp (the top of scarp marked by red arrows) of 3–4 m on Fan1 east of the Jilglang River. (c) Photograph taken facing approximately NW showing the fault scarp (the top of scarp marked by the red arrow) of 5–6 m on Fan2 west of the Jilglang River.

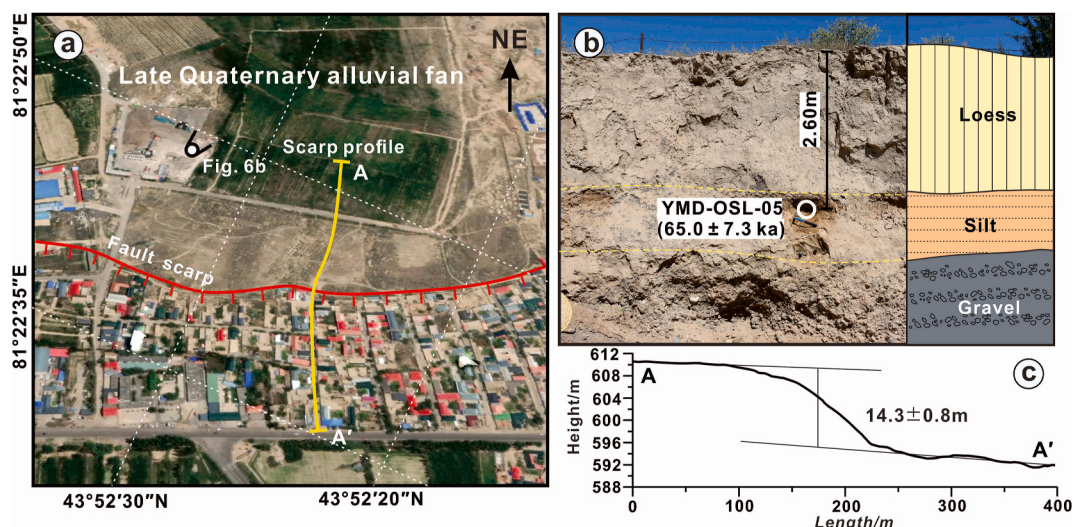


Fig. 6. (a) High-resolution remote sensing image (derived from Google Earth) showing a well-expressed linear trace along the southern branch of the YF west of the Jilglang River. (b) Photograph taken facing approximately NE, showing the sediments of the alluvial fan and the sample location of YMD-OSL-05. (c) Topographic profile across the southern branch fault scarp showing a vertical displacement of ~14.3 m (see Fig. 6a for the location).

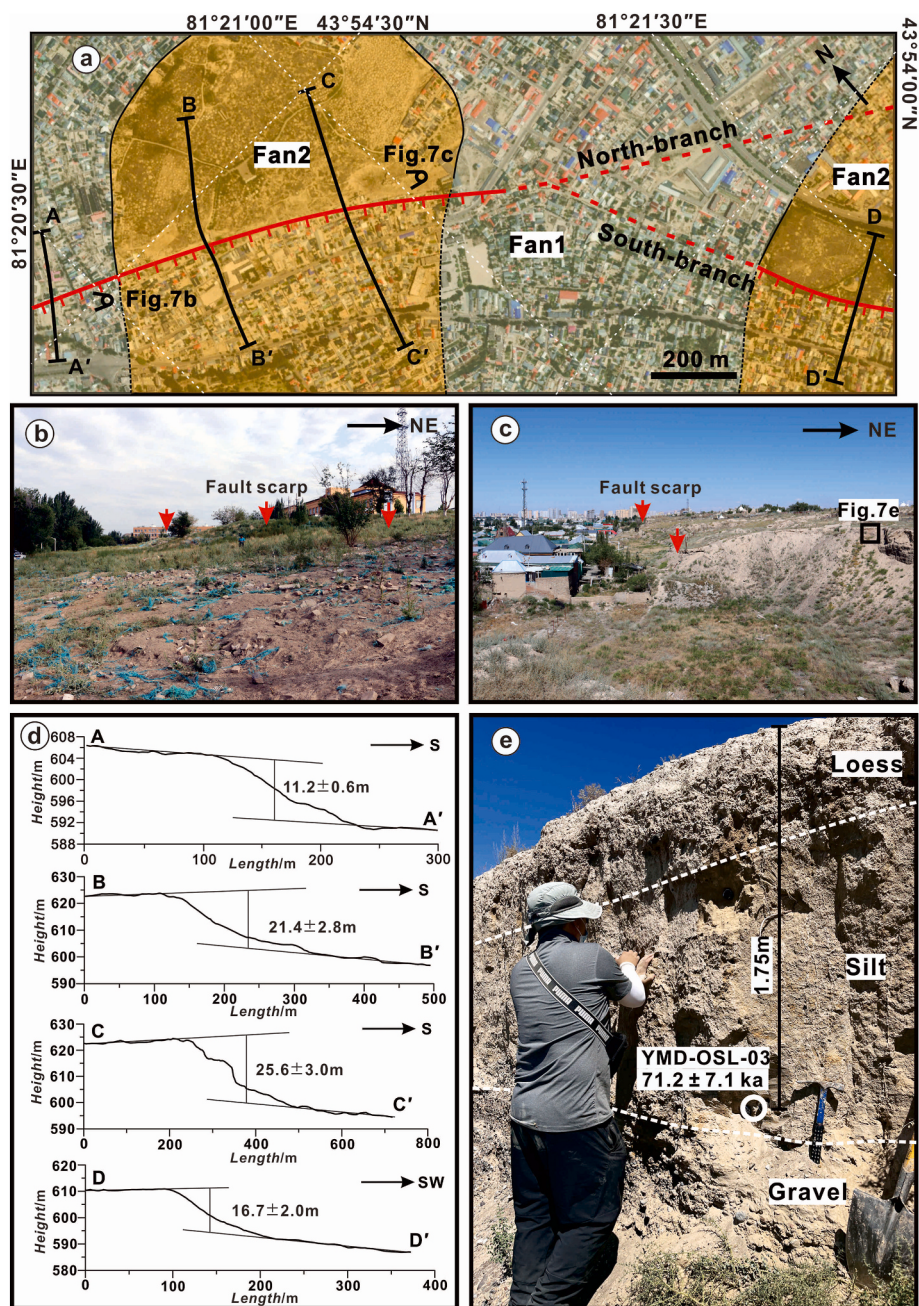


Fig. 7. (a) High-resolution remote sensing image (derived from Google Earth) showing the fault geometry of the YF in the city of Yining. (b) Photograph showing the SW-facing scarp (marked by red arrows) on the alluvial fan of Fan1. (c) Photograph showing the SW-facing scarp (marked by red arrows) on the alluvial fan of Fan2. (d) Topographic profiles across the scarp showing the vertical displacements of the alluvial fans (see Fig. 7a for the locations). (e) Photograph taken facing approximately NW showing the sediments of alluvial fan Fan2 and the sample location of YMD-OSL-03.

Table 1
OSL sampling results for the Yamadu fault.

Sample number	Sample site (cm)	Depth content	Moisture (ppm)	U (ppm)	Th (%)	K dose rate (Gy/ka)	Environmental dose (Gy)	Equivalent (ka)	OSL age protocol	measurement
YMD-OSL-01	43°38'33.4"N 81°41'11.9"E	330	10 %	3.08	12.22	3.54	5.3 ± 0.3	555.8 ± 42.2	104.7 ± 9.4	Coarse-grained potassium feldspar
YMD-OSL-02	43°38'30.7"N 81°41'16.5"E	190	10 %	3.97	13.23	2.19	4.1 ± 0.2	169.9 ± 2.1	41.9 ± 3.4	Fine-grained quartz
YMD-OSL-03	43°54'22.4"N 81°20'59.6"E	180	10 %	7.05	10.2	1.99	4.4 ± 0.2	311.5 ± 28.6	71.2 ± 7.1	Fine-grained quartz
YMD-OSL-05	43°52'32.8"N 81°22'51.9"E	260	10 %	4.48	11.46	1.73	3.6 ± 0.1	234.6 ± 24.6	65.0 ± 7.3	Fine-grained quartz

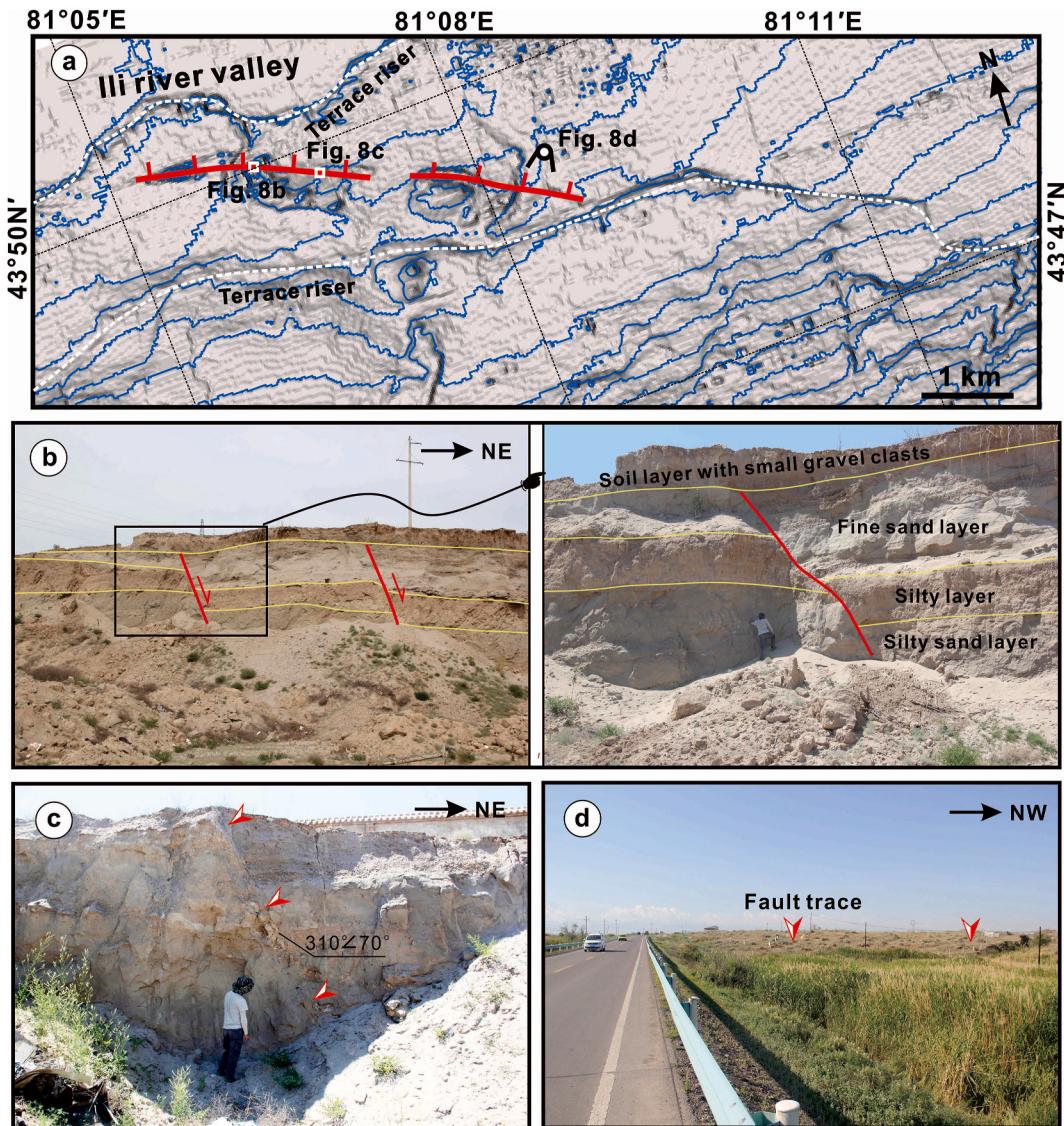


Fig. 8. (a) Copernicus WorldDEM with a resolution of 30 m (the unannotated image is provided in the supplement) showing the geometry of the secondary normal fault on the river terrace of the Ili River near Qapqal County. (b, c) Photographs showing the northeast-down fault sections. The secondary fault is a high-angle normal fault dipping NE at 70–75° (marked by red arrows). (d) Photograph showing the NE-facing scarp (marked by red arrows) west of Yindeng South Road.

section. Near the northwestern end of the fault, a gravel quarry reveals that the secondary fault is composed of two NE-dipping fault branches and displaced the late-Pleistocene sandy gravel layer with a total vertical displacement of approximately 3–4 m (Fig. 8b). Southeastward ~1 km along the fault strike from the gravel quarry, we cleaned a natural outcrop perpendicular to the strike of the NE-facing scarp; at this outcrop, a normal fault dipping steeply northeast with dip angles of ~70–75° was also revealed (Fig. 8c). The height of the topographic bulge decreases gradually southeastward along the fault strike. To the west of Yindeng South Road, fault traces disappear at the surface (Fig. 8d).

4.3. Slip rate of the YF

In the previous sections, we quantified the vertical displacements of different geomorphic surfaces along the fault strike. The OSL dating results (Table 1) can be used to accurately define geomorphic surface ages. At Site 2, we measured the vertical displacement of the fault to be 15.2 ± 2.0 m at the alluvial fan and 9.1 ± 1.8 m at the T2 terrace. The age of 104.7 ± 9.4 ka determined from the OSL sample of YMD-OSL-01

represents the maximum age of the alluvial fan. The depositional age of 41.9 ± 3.4 ka determined from YMD-OSL-02 also represents the maximum age of the T2 terrace at Site 2. Based on the vertical displacements and corresponding dating results at Site 2, we obtained a vertical slip rate of 0.15 ± 0.03 mm/yr for the last 105 ka and 0.22 ± 0.06 mm/yr for the last 42 ka. Thus, we determined an average vertical slip rate of 0.20 ± 0.08 mm/yr at Site 2.

At Site 3, the YF is composed of two fault branches. On the piedmont alluvial Fan2 to the west of the Jilglang River, we measured a vertical displacement of 14.3 ± 0.8 m across the southern branch and approximately 5–6 m across the northern branch. Thus, the total vertical displacement of the YF on Fan2 is approximately 18.5–21.1 m when the uncertainty is uniformly distributed. The age of 65.0 ± 7.3 ka determined from the OSL sample of YMD-OSL-05 represents the minimum age of this geomorphic surface. We therefore can determine the vertical slip rate to be 0.31 ± 0.05 mm/yr at Site 3. At Site 4, we measured a maximum vertical displacement of 25.6 ± 3.0 m at the Fan2 surface. The depositional age determined by YMD-OSL-03 is 71.2 ± 7.1 ka, which represents the maximum age of this alluvial fan. Thus, the vertical slip rate of the YF is 0.37 ± 0.08 mm/yr at Site 4, which is the

northwesternmost extent of the fault.

The fault dip angle near the surface revealed by the fault sections is $\sim 60\text{--}70^\circ$ (Fig. 3b and c). Given a consistent fault dip angle (θ) along the YF, the fault vertical slip rate (v) and the extension rate (s) can be approximately formulated as $s = v/\tan \theta$. Thus, we obtained extension rates of $0.10 \pm 0.06 \text{ mm/yr}$, $0.15 \pm 0.06 \text{ mm/yr}$ and $0.19 \pm 0.08 \text{ mm/yr}$ at Site 2, Site 3 and Site 4, respectively.

5. Discussion and implications

Late Cenozoic deformation associated with the ongoing India–Eurasia collision in the Tian Shan orogenic belt was dominated by overthrusting of the Paleozoic bedrock upon the foreland and/or intermontane basins (Avouac et al., 1993; Burchfiel et al., 1999; Deng et al., 2000; Fu et al., 2003; Tapponnier and Molnar, 1979; Thompson et al., 2002; Yin et al., 1998; Zhang et al., 1996). Within foreland/intermontane basins, roughly E–W-striking faults are usually dominated by thrust faulting and are interpreted as splay branches in the upper crust that propagate from the range-front structure (e.g., Deng et al., 2000; Grützner et al., 2019; Mackenzie, 2016). However, our field investigations and analysis of fault kinematics indicate that the overall motion of the NW-striking YF in the Ili Basin interior has been characterized by normal faulting instead of the expected thrust motion (Luo et al., 2003). In the compressive region, normal faults are usually interpreted as bending moment structures resulting from tensile stresses along the anticlinal crest of the fold (Yeats et al., 1997). However, a NW-trending fold is not present in the Ili Basin. We therefore suggest that the YF is not a secondary structure related to anticlines. The vertical displacements of normal faulting clearly vary along the fault strike. The vertical slip rate of $0.37 \pm 0.08 \text{ mm/yr}$ in the city of Yining, the northwesternmost extent of the fault, is significantly greater than that obtained near the town of Yamadu ($0.20 \pm 0.08 \text{ mm/yr}$) along the northwestern segment of the YF (Fig. 9). Approximately 15 km

southeastward from Yamadu, the fault traces disappear in the late-Pleistocene alluvial fan, indicating a southeastward decrease in the deformation rate along the fault strike. The secondary NE-dipping normal fault near Qapqal County displays a dip opposite to that of the YF and extends only $\sim 5 \text{ km}$ long. We speculate that the secondary NE-dipping normal fault is an antithetic structure of the SW-dipping YF.

For the Ili block, its boundary structures of right-lateral faulting to the north (Wu et al., 2020) and northward thrust faulting to the south (Grützner et al., 2017) result in counterclockwise rotation motion, as indicated by present-day GPS measurements (e.g., Wu et al., 2021; Zubovich et al., 2010). We suggest that the YF represents a boundary fault accommodating the relative divergence between the Ili block and Tian Shan Mountains. Thus, there might be local westward extension in the Tian Shan region (Wu et al., 2021; Zubovich et al., 2010), despite the dominance of thrust faulting shown by fault plane solutions of nearly all earthquakes in the region. Because of the counterclockwise rotation, the westward motion in the north is greater than that in the southern Ili Basin, which causes a gradual increase in the vertical slip rate from southeast to northwest along the normal YF, as verified in this study. Assuming that the extension rate of approximately 0.2 mm/yr determined at the northwestern end of the YF represents extensional deformation within the Ili Basin interior, we can roughly calculate a counterclockwise rotation rate of $\sim 0.16^\circ/\text{Ma}$ for the Ili Basin around a pole near the southeastern end of the YF (Fig. 9). Unlike the outward motion of crustal materials within the plateau and vortex motion characterized by continuous deformation around the Eastern Himalaya Syntax (Zhang et al., 2004), our results indicate that the Ili block rotates around a pole and shows a regular increase with increasing rotation radius (Wu et al., 2021), displaying a block-like pattern of deformation (Thompson et al., 2002). Thus, active deformation related to the India–Eurasia collision in the Tian Shan region is composed of N–S crustal shortening and vertical uplift of weak lithospheric mountains, as well as block rotation and lateral extrusion of rigid intermountain

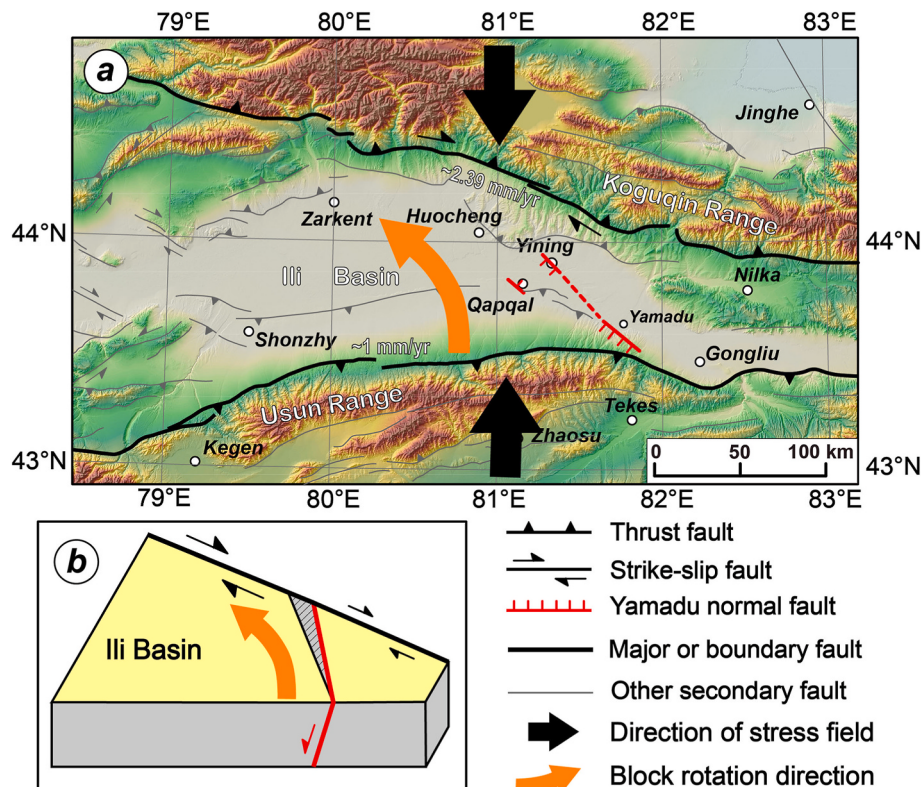


Fig. 9. (a) The triangular Ili block bounded by a right-lateral fault on the north and a northward thrust fault on the south rotates counterclockwise around the vertical axes, which accommodates the N–S convergence related to the ongoing India–Eurasia collision. (b) Model showing that the NW-striking YF presents normal faulting to accommodate relative divergence between the Ili block and Tian Shan Mountains caused by counterclockwise rotation of the rigid Ili block.

basins.

The Ili Basin with Precambrian basement (Pelsmaeker et al., 2015) is the relict of a stronger block embedded in weaker units (Charvet et al., 2011) and includes several fragments of Paleozoic microcontinents and amalgamated island arcs (Zhang et al., 1984; Allen et al., 1993; Sengör et al., 1993; Heubeck, 2001; Windley et al., 2007; Gao et al., 2009; Charvet et al., 2011). Compared with the surrounding strongly deformed ranges, the wide and low relief in the Ili Basin implies that the strong Ili lithosphere mainly deforms at its margins (Grützner et al., 2019; Wu et al., 2020). With the Cenozoic deformation resulting from rapid uplift of the surrounding mountains with elevations greater than 4000 m (Wu et al., 2020), the isotherms within the lithosphere then stretched downward, which changed the localized lithospheric convection of the Ili block (Morency et al., 2002; Geron et al., 2024). Thus, the relatively strong Ili block progressively removed cratonic keels and broke up cratonic continental fragments. Lateral extrusion caused by the strike-slip boundary structures of the basin results in E–W-oriented tensile stress, which destroys the basement of the Ili Basin that is subjected to compressive stress (Feng et al., 1989). The Ili block may have entered a stage where it is easier to deform the interior along some inherited structures or preexisting weak zones (Grützner et al., 2019). Although normal faults have been widely observed in the intra-continental compression orogenic belts, such as the southern Tibet and the Aegean in the Mediterranean (Tapponnier et al., 1981), normal faulting in an intermountain basin interior was rarely reported. Our study shows that a strong lithospheric block within the continent ultimately may be crushed and/or weakened and reactivated. In an intra-continental compression orogenic belt, with the rapid uplift of ranges, the stronger block trapped between weaker units is likely to deform the interior rather than further uplift the surrounding ranges (Tapponnier et al., 1981; Grützner et al., 2019).

6. Conclusions

The NW-striking YF in the interior of the Ili Basin extends ~70 km in length. The well-expressed linear traces on the remote sensing images and the displaced late Quaternary geomorphic surfaces along the fault attest to its strong activity during the late Quaternary. Detailed interpretations of high-resolution remote sensing images, field observations, and mapping results reveal that the YF is a high-angle normal fault and exhibits a southeastward decrease in deformation rate along its strike. By surveying the deformed geomorphic surfaces with a UAV and geochronological dating via the OSL method, we obtained a maximum late Quaternary vertical slip rate of 0.37 ± 0.08 mm/yr and an E–W extension rate of 0.19 ± 0.08 mm/yr at the northwesternmost extent of the fault.

The YF represents a boundary fault accommodating the relative divergence between the Ili block and Tian Shan Mountains. The rigid Ili Basin rotated counterclockwise at a rate of $\sim 0.16^\circ/\text{Ma}$ around a pole near the southeastern end of the YF. Our study indicates that in addition to the overwhelming crustal shortening, lateral extrusion and block rotation of the rigid microcontinents embedded in the mountains are important components for accommodating the N–S convergence associated with the ongoing India–Eurasia collision.

Credit author statement

A statement on the respective roles of each author: Chuanyong Wu: Conceptualization, Funding acquisition, Methodology, Investigation, Writing-original draft, Writing-review & editing. Haiyang Yuan: Formal analysis, Methodology, Data curation. Kezhi Zang: Investigation, Data curation, Visualization. Sihua Yuan: Investigation. Xiangdong Bai: Investigation. Chengyao Guan: Investigation. Peizhen Zhang: Funding acquisition. Zhan Gao: Formal analysis. Xuezhu Wang: Formal analysis.

Declaration of competing interest

The authors declare that they have no known competing financial interests or personal relationships that could have appeared to influence the work reported in this paper.

Acknowledgments

This research is supported by the National Natural Science Foundation of China (42272258, 42030301), the Fundamental Research Funds for the Central Universities (ZY20220205) and the Second Tibetan Plateau Scientific Expedition and Research Program (STEP) (2019QZKK0901). We thank the State Key Laboratory of Earthquake Dynamics, CEA and H.L. Yang for their help in the interpretation and dating of the OSL samples. Partial high-resolution remote sensing images were obtained from Google Earth. The Copernicus WorldDEM is archived by the European Space Agency (<https://spacedata.copernicus.eu/collections/copernicus-digital-elevation-model>). We thank the anonymous reviewer and the editor for their detailed and constructive comments and suggestions, which helped improve the manuscript.

Appendix A. Supplementary data

Supplementary data to this article can be found online at <https://doi.org/10.1016/j.quascirev.2025.109600>.

Data availability

All data and/or code is contained within the submission.

References

- Aitken, M.J., 1998. An Introduction to Optical Dating: the Dating of Quaternary Sediments by the Use of Photon-Stimulated Luminescence. Oxford University Press, New York.
- Allen, M.B., Windley, B.F., Zhang, C., 1993. Palaeozoic collisional tectonics and magmatism of the Chinese Tianshan, central Asia. *Tectonophysics* 220, 89–115.
- Avouac, J.P., Tapponnier, P., 1993. Kinematic model of active deformation in central Asia. *Geophys. Res. Lett.* 20, 895–898. <https://doi.org/10.1029/93GL00128>.
- Avouac, J.P., Tapponnier, P., Bai, M.X., You, H.C., Wang, G., 1993. Active faulting and folding in the northern Tianshan and rotation of Tarim relative to Dzungarian and Kazakhstan. *J. Geophys. Res.* 98, 6755–6804.
- Burchfiel, B., Brown, E.T., Deng, Q.D., Feng, X.Y., Li, J., Molnar, P., Shi, J.B., Wu, Z.M., You, H.C., 1999. Crustal shortening on the margins of the Tien Shan, Xinjiang, China. *Int. Geol. Rev.* 41, 665–700.
- Burtman, V.S., 1975. Structural geology of the Variscan Tien Shan. *Am. J. Sci.* 280, 725–744.
- Buylaert, J.P., Thiel, C., Murray, A.S., Vandenberghe, D.A.G., Yi, S., Lu, H., 2011. IRSL and post-IR IRSL residual doses recorded in modern dust samples from the Chinese Loess Plateau. *Geochronometria* 38, 432–440.
- Charvet, J., Shu, L., Laurent-Charvet, S., Wang, B., Faure, M., Cluzel, D., Chen, Y., Jong, K.D., 2011. Palaeozoic tectonic evolution of the Tianshan belt, NW China. *Sci. China Earth Sci.* 54, 166–184. <https://doi.org/10.1007/s11430-010-4138-1>.
- Cording, A., Hetzel, R., Kober, M., Kley, J., 2014. ^{10}Be exposure dating of river terraces at the southern mountain front of the Dzungarian Alatau (SE Kazakhstan) reveals rate of thrust faulting over the past ~400 ka. *Quat. Res. (Tokyo)* 81 (1), 168–178. <https://doi.org/10.1016/j.yqres.2013.10.016>.
- Deng, Q.D., Feng, X.Y., Zhang, P.Z., Xu, X.W., Peng, S.Z., Li, J., 2000. Active Tectonics of Tianshan. Seismological Press, Beijing, pp. 302–321 (in Chinese).
- Duller, G.A.T., 2003. Distinguishing quartz and feldspar in single grain luminescence measurements. *Radiat. Meas.* 37, 161–165.
- England, P., Houseman, G., 1985. Role of lithospheric strength heterogeneities in the tectonics of Tibet and neighbouring regions. *Nature* 315, 297–301. <https://doi.org/10.1038/315297a0>.
- Feng, X.Y., 1997. The Paleoearthquakes in Xinjiang Region. Sci-Tech and Public Health Press of Xinjiang, Urumqi (in Chinese).
- Feng, Y., Coleman, R.G., Tilton, G., Xiao, X., 1989. Tectonic evolution of the west Junggar region, Xinjiang, China. *Tectonics* 8, 729–752.
- Fu, B., Lin, A., Kano, K.I., Maruyama, T., Guo, J., 2003. Quaternary folding of the eastern Tian Shan, northwest China. *Tectonophysics* 369 (1–2), 79–101. [https://doi.org/10.1016/S0040-1951\(03\)00137-9](https://doi.org/10.1016/S0040-1951(03)00137-9).
- Gao, J., Long, L.L., Klemd, R., Qian, Q., Liu, D.Y., Xiong, X.M., Su, W., Liu, W., Wang, Y.T., Yang, F.Q., 2009. Tectonic evolution of the South Tianshan orogen and adjacent regions, NW China: geochemical and age constraints of granitoid rocks. *Int. J. Earth Sci.* 98 (6), 1221–1238. <https://doi.org/10.1007/s00531-008-0370-8>.

- Gebhardt, A.C., Naudts, L., de Mol, L., Klerkx, J., Abdakhmatov, K., Sobel, E.R., de Batist, M., 2017. High-amplitude lake-level changes in tectonically active Lake Issyk-Kul (Kyrgyzstan) revealed by high-resolution seismic reflection data. *Clim. Past* 13 (1), 73–92. <https://doi.org/10.5194/cp-13-73-2017>.
- Gernon, T.M., Hincks, T.K., Brune, S., Braun, J., Jones, S.M., Keir, D., Cunningham, A., Glerun, A., 2024. Coevolution of craton margins and interiors during continental break-up. *Nature* 632, 327–335. <https://doi.org/10.1038/s41586-024-07717-1>.
- Goode, J.K., Burbank, D.W., Ormukov, C., 2014. Pliocene-Pleistocene initiation, style, and sequencing of deformation in the central Tien Shan. *Tectonics* 33 (4), 464–484. <https://doi.org/10.1002/2013TC003394>.
- Grützner, C., Carson, E., Walker, R.T., Rhodes, E., Mukambayev, A., Moldobaev, A., et al., 2017. Assessing the activity of faults in continental interiors: palaeoseismic insights from SE Kazakhstan. *Earth Planet Sci. Lett.* 459, 93–104. <https://doi.org/10.1016/j.epsl.2016.11.025>.
- Grützner, C., Campbell, G., Walker, R.T., Jaskson, J., Mackenzie, D., Abdakhmatov, K., Mukambayev, A., 2019. Shortening accommodated by thrust and strike-slip faults in the Ili Basin, northern Tien Shan. *Tectonics* 38, 2255–2274. <https://doi.org/10.1029/2018TC005459>.
- Han, X.Z., Li, S.X., Zheng, E.J., Li, X.G., Cai, Y.Q., Chen, Z.L., 2004. Neotectonic activity characteristics of Yili Basin and its relation to the formation of sandstone-type uranium deposits. *Xinjiang Geol.* 22, 378–381 (in Chinese with English abstract).
- Hendrix, M.S., Dumitru, T.A., Graham, S.A., 1994. Late oligocene-early Miocene unroofing in the Chinese Tianshan: an early effect of the India-Asia collision. *Geology* 22 (6), 487–490. [https://doi.org/10.1130/0091-7613\(1994\)022<487:LOEMUI>2.3.CO;2](https://doi.org/10.1130/0091-7613(1994)022<487:LOEMUI>2.3.CO;2).
- Heubeck, C., 2001. Assembly of central Asia during the middle and late Paleozoic. In: Hendrix, M.S., Davis, G.A. (Eds.), *Paleozoic and Mesozoic Tectonic Evolution of Central Asia: from Continental Assembly to Intracontinental Deformation*, vol. 194. Geological Society of America Memoir, Boulder, Colorado, pp. 1–22.
- Kober, M., Seib, N., Kley, J., Voigt, T., 2013. Thick-skinned thrusting in the northern Tien Shan foreland, Kazakhstan: structural inheritance and polyphase deformation. *Geolog. Soc.* 377, 19–42. <https://doi.org/10.1144/SP377.7>. London: Special Publications.
- Liu, J.F., Chen, J., Yin, J.H., Lu, Y.C., Murray, A., Chen, L.C., Thomposn, J., Yang, H.L., 2010. OSL and AMS ^{14}C dating of the penultimate earthquake at the Leigu trench along the Beichuan Fault, Longmenshan, in the northeast margin of the Tibetan plateau. *Bull. Seismol. Soc. Am.* 100 (5B), 2681–2688.
- Lu, Y.C., Wang, X.L., Wintle, A.G., 2007. A new OSL chronology for dust accumulation in the last 130,000 yr for the Chinese Loess Plateau. *Quat. Res. (Tokyo)* 67, 152–160.
- Luo, F., Bai, M., Chen, J., 2003. Study on new activity characteristics of the active faults in Yining Basin of Xinjiang. *Inland Earthq.* 17, 4–10 (in Chinese with English abstract).
- Mackenzie, D., 2016. Active Shortening in the Alpine-Himalayan Belt (Phd Thesis). University of Oxford, Oxford, UK.
- Molnar, P., Tapponniere, P., 1981. A possible dependence of tectonic strength on the age of the crust in Asia. *Earth Planet Sci. Lett.* 52, 107–114.
- Morency, C., Doin, M.P., Dumoulin, C., 2002. Convective destabilization of a thickened continental lithosphere. *Earth Planet Sci. Lett.* 202 (2), 303–320. [https://doi.org/10.1016/S0012-821X\(02\)00753-7](https://doi.org/10.1016/S0012-821X(02)00753-7).
- Pelsmaeker, E.D., Glorie, S., Buslov, M.M., Zhimulev, F.I., Poujol, M., Korobkin, V.V., Vanhaecke, F., Petrov, E.V., Grave, J.D., 2015. Late-Paleozoic emplacement and Meso-Cenozoic reactivation of the southern Kazakhstan granitoid basement. *Tectonophysics* 662, 416–433. <https://doi.org/10.1016/j.tecto.2015.06.014>.
- Sengör, A.M.C., Natal'In, B.A., Burtman, V.S., 1993. Evolution of the Altai tectonic collage and Palaeozoic crustal growth in Eurasia. *Nature* 364, 299–307. <https://doi.org/10.1038/364299a0>.
- Sobel, E.R., Chen, J., Heermance, R.V., 2006. Late Oligocene-Early Miocene initiation of shortening in the southwestern Chinese Tian Shan: implications for Neogene shortening rate variations. *Earth Planet Sci. Lett.* 247 (1–2), 70–81. <https://doi.org/10.1016/j.epsl.2006.03.048>.
- Tapponniere, P., Molnar, P., 1979. Active faulting and Cenozoic tectonics of the Tien Shan, Mongolia, and Baykal regions. *J. Geophys. Res.* 84, 3245–3459. <https://doi.org/10.1029/JB084iB07p03425>.
- Tapponniere, P., Mercier, J.L., Armijo, R., Tonglin, H., Ji, Z., 1981. Field evidence for active normal faulting in Tibet. *Nature* 294 (5840), 410–414. <https://doi.org/10.1038/294410a0>.
- Thompson, S.C., Weldon, R.J., Rubin, C.M., Abdakhmatov, K., Molnar, P., Berger, G.W., 2002. Late Quaternary slip rates across the central Tien Shan, Kyrgyzstan, central Asia. *J. Geophys. Res.* 107 (B9), 2203. <https://doi.org/10.1029/2001JB000596>.
- Wang, M., Shen, Z.K., 2020. Present-day crustal deformation of continental China derived from GPS and its tectonic implications. *J. Geophys. Res. Solid Earth* 125. <https://doi.org/10.1029/2019JB018774>.
- Wang, B., Shu, L.S., Cluzel, D., Faure, M., Charvet, J., 2007. Geochemical constraints on Carboniferous volcanic rocks of the Yili Block (Xinjiang, NW China): implication for the tectonic evolution of Western Tianshan. *J. Asian Earth Sci.* 29, 148–159. <https://doi.org/10.1016/j.jseas.2006.02.008>.
- Wang, Q., Nie, X., Wu, C., 2013. Mid-and short-term anomaly characteristics on seismicity before the two M6.0 earthquakes in northern Tianshan Mountains since 2011. *Earthq. Res. China* 29 (4), 448–461 (in Chinese with English abstract).
- Westoby, M.J., Brasington, J., Glasser, N.F., Hambrey, M.J., Reynolds, J.M., 2012. ‘Structure-from-motion’ photogrammetry: a lowcost, effective tool for geoscience applications. *Geomorphology* 179, 300–314. <https://doi.org/10.1016/j.geomorph.2012.08.021>.
- Windley, B.F., Allen, M.B., Zhang, C., Zhao, Z.Y., Wang, G.R., 1990. Paleozoic accretion and Cenozoic redeformation of the Chinese Tien Shan range, central Asia. *Geology* 18, 128–131.
- Windley, B.F., Alexeev, D., Xiao, W., Kröner, A., Badarch, G., 2007. Tectonic models for accretion of the Central Asian Orogenic Belt. *J. Geol. Soc. London* 164 (1), 31–47. <https://doi.org/10.1144/0016-76492006-022>.
- Wu, C.Y., Ren, G., Yu, J., Zheng, W., Li, X., Liu, J., Wang, S., Li, C., Zhang, Z., Yang, H., Zhang, D., 2020. Oblique right-lateral faulting along the northern margin of the Ili Basin in the northern Tian Shan, Northwest China. *Tectonics* 39, e2020TC006061. <https://doi.org/10.1029/2020TC006061>.
- Wu, C.Y., Wang, W.T., Zheng, W.J., Zhang, P.Z., Yu, Z.Y., 2021. Opposite sense of strike-slip faulting and crustal rotation accommodating left-lateral shear between the tianshan Mountains and Kazakh platform. *Geophys. Res. Lett.* 48, e2021GL096442. <https://doi.org/10.1029/2021GL096442>.
- Wu, C.Y., Zhang, P.Z., Zhang, Z.Q., Zheng, W.J., Xu, B.B., Wang, W.T., Yu, Z.Y., Dai, X.Y., Zhang, B.X., Zang, K.Z., 2023. Slip partitioning and crustal deformation patterns in the Tianshan orogenic belt derived from GPS measurements and their tectonic implications. *Earth Sci. Rev.* 238, 104362. <https://doi.org/10.1016/j.earscirev.2023.104362>.
- Wu, C.Y., Zheng, W., Zhang, P., Zhang, Z., Jia, Q., Yu, J., Zhang, H., Yao, Y., Liu, J., Han, G., Chen, J., 2019. Oblique thrust of the Maidan fault and late Quaternary tectonic deformation in the southwestern Tian Shan, Northwestern China. *Tectonics* 38 (8), 2625–2645. <https://doi.org/10.1029/2018TC005248>.
- Xiao, W.J., Windley, B.F., Sun, S., Li, J.L., Han, B.C., Han, C.M., Yuan, C., Sun, M., Chen, H.L., 2015. A tale of amalgamation of three permo-triassic collage systems in central Asia: oroclines, sutures, and terminal accretion. *Annu. Rev. Earth Planet Sci.* 43 (1), 477–507. <https://doi.org/10.1146/annurev-earth-060614-105254>.
- Yang, S.M., Li, J., Wang, Q., 2008. The deformation pattern and fault rate in the Tianshan Mountains inferred form GPS observations. *Sci. China E* 51 (8), 1064–1080. <https://doi.org/10.1007/s11430-008-0090-8>.
- Yang, H.L., Chen, J., Porat, N., Li, T., Li, W.Q., Xiao, W.P., 2017. Coarse versus Fine-grain quartz optical dating of the sediments related to the 1985 Ms7.1 Wuqia earthquake, Northeastern margin of the Pamir salient, China. *Geochronometria* 44, 299–306.
- Yeats, R.S., Sieh, K., Allen, C.R., 1997. *The Geology of Earthquake*. Oxford University Press, Oxford, UK, p568.
- Yin, A., Nie, S., Craig, P., Harrison, T.M., Ryerson, F.J., Qian, X.L., Yang, G., 1998. Late Cenozoic tectonic evolution of the southern Chinese Tianshan. *Tectonics* 17 (1), 1–27. <https://doi.org/10.1029/97TC03140>.
- Yin, G.H., Jiang, J.X., Pei, H.D., 2006. The fault and the maximal displacement of Nileke earthquake in 1812. *Inland Earthq.* 20 (4), 296–304 (in Chinese with English abstract).
- Zhang, Z.M., Liou, J.G., Coleman, R.G., 1984. An outline of the plate tectonics of China. *Geol. Soc. Am. Bull.* 95 (3), 295–312. [https://doi.org/10.1130/0016-7606\(1984\)95<295:AOTPPT>2.0.CO;2](https://doi.org/10.1130/0016-7606(1984)95<295:AOTPPT>2.0.CO;2).
- Zhang, P.Z., Deng, Q.D., Yang, X.P., Peng, S.Z., Xu, X.W., Feng, X.Y., 1996. Late Cenozoic tectonic deformation and mechanism along the Tianshan Mountain, North Western China. *Earthq. Res. China* 12 (2), 127–140 (in Chinese with English abstract).
- Zhang, G.W., Li, S.Z., Liu, J.X., Teng, Z.H., Jin, H.L., Li, W., Huang, X.X., Wu, Y.H., 1999. Structural feature and evolution of Yili Basin, Xinjiang. *Earth Sci. Front.* 6 (4), 203–214 (in Chinese with English abstract).
- Zhang, P.Z., Shen, Z.K., Wang, M., Gan, W.J., Bürgmann, R., Molnar, P., Wang, Q., Niu, Z.J., Sun, J., Wu, J., 2004. Continuous deformation of the Tibetan Plateau from global positioning system data. *Geology* 32 (9), 809–812.
- Zubovich, A.V., Wang, X.Q., Scherba, Y.G., Schelochkov, G.G., Reilinger, R., Reigber, C., et al., 2010. GPS velocity field for the Tien Shan and surrounding regions. *Tectonics* 29, TC6014. <https://doi.org/10.1029/2010TC002772>.